Geochemistry Geophysics Geosystems G3

Article
Volume 14, Number 3
7 March 2013
doi:10.1002/ggge.20057
ISSN: 1525-2027

Published by AGU and the Geochemical Society

The large-scale surface uplift in the Altiplano-Puna region of Bolivia: A parametric study of source characteristics and crustal rheology using finite element analysis

James Hickey, Joachim Gottsmann, and Rodrigo del Potro

University of Bristol, School of Earth Sciences, Wills Memorial Building, Queens Road, Bristol, BS8 1RJ, UK (james.hickey@bristol.ac.uk)

[1] This paper focuses on the driving mechanism behind a 70 km wide region of ground uplift centered on Uturuncu volcano, in the Altiplano-Puna region of southern Bolivia. We present a series of forward models using finite element analysis to simultaneously test for first-order parameters that help constrain a viable model for the observed maximum line of sight uplift rate of 1–2 cm/yr between 1992 and 2006. Stresses from pressure sources with finite geometries are solved numerically, accounting for both homogeneous and heterogeneous mechanical rock properties in elastic and viscoelastic rheologies. Crustal heterogeneity is constrained by seismic velocity data that indicate the presence of a large low-velocity zone, the Altiplano-Puna magma body, at depths of ~17 km below the surface. A viscoelastic rheology is employed to account for time-dependent deformation and an inelastic crust. Comparing homogeneous and heterogeneous models demonstrates the significant impact of a mechanically weak, source-depth layer, which alters surface displacement patterns by buffering subsurface deformation. Elastic model results guide the source parameters tested in the viscoelastic models and demonstrate a range of possible causative source geometries. Our preferred model suggests that pressurization of a magma source extending upward from the Altiplano-Puna magma body is causing the observed surface uplift and alludes to a continued increase in this pressure to explain both the spatial and temporal patterns. We also demonstrate how a pressure-time function plays a first-order role in explaining the observed temporal deformation pattern.

Components: 9,100 words, 11 figures, 5 tables.

Keywords: Finite Element Analysis; Uturuncu; ground deformation; crustal mechanics; volcanic unrest.

Index Terms: 8439 Volcanology: Physics and chemistry of magma bodies; 3225 Mathematical Geophysics: Numerical approximations and analysis (4260); 8419 Volcanology: Volcano monitoring (4302, 7280)

Received 24 October 2012; **Revised** 19 December 2012; **Accepted** 20 December 2012; **Published** 7 March 2013.

Hickey, J., J. Gottsmann, and R. del Potro (2013), The large-scale surface uplift in the Altiplano-Puna region of Bolivia: A parametric study of source characteristics and crustal rheology using finite element analysis, *Geochem. Geophys. Geosyst.*, *14*, 540–555, doi:10.1002/ggge.20057.

1. Introduction and Background

[2] Volcano geodesy examines the spatial and temporal patterns of volcanic surface deformation, with the aim of locating causative sources and constraining their characteristics [e.g., *Dvorak and Dzurisin*, 1997]. When combined with other geophysical and geochemical methods, this can provide a basis for determining unrest and eruption forecasting [e.g., *Poland et al.*, 2006]. However, making the transition from geodetic data to subsurface source processes requires the use of nonunique geodetic models, which demand

assumptions about mechanical parameters. This can lead to oversimplifications and erroneous or unrealistic predictions as a result of the trade-offs between subsurface mechanics and source characteristics.

[3] Volcanic deformation models have been continually improving since the advent of the first analytical models, whereby a pressurized point source is situated in an isotropic, homogeneous, elastic half-space [*Anderson*, 1936; *Mogi*, 1958]. Such improvements have accounted for finite source shapes [*Davis*, 1986; *McTigue*, 1987; *Yang et al*., 1988; *Fialko et al*., 2001] and viscoelastic behavior [*Dragoni and Magnanensi*, 1989; *Segall*, 2010]. Numerical methods have also been applied, and while finite element analysis is not a new technique in volcano geodesy [*Dieterich and Decker*, 1975], its use has been expanding in recent years utilizing its flexibility and capability to solve for geological complexities beyond the analytical realm. Models have been developed to test for the influence of topography [*Williams and Wadge*, 1998], source multiplicity [*Geyer and Gottsmann*, 2010; *Hautmann et al*., 2010], subsurface heterogeneity [*Folch and Gottsmann*, 2006; *Currenti et al*., 2007; *Manconi et al*., 2007; *Masterlark*, 2007; *Geyer and Gottsmann*, 2010; *Hautmann et al*., 2010], viscoelasticity [*Newman et al*., 2001, 2006; *Del Negro et al*., 2009], and elasto-plasticity [*Trasatti et al*., 2005; *Scandura et al*., 2009; *Currenti et al*., 2010] on the deformation pattern, but they are seldom tested simultaneously. The latter three approaches have found that accounting for more realistic subsurface conditions, in terms of crustal structure and rheology, results in more realistic pressure changes (i.e., smaller excess pressures compared to homogeneous, isotropic, and elastic solutions).

[4] This study focuses on one of the largest regions of coherent volcanic ground deformation ever recorded, centered on Uturuncu volcano in Southern Bolivia (Figure 1) and identified using interferometric synthetic aperture radar (InSAR) [*Pritchard and Simons*, 2002]. Uturuncu volcano is a dacitic stratovolcano, which appears to have been active between 890 ka and 270 ka [*Sparks et al*., 2008]. It is located in southwest Bolivia (22°16′12″S, 67°10′48″W) within the Altiplano-Puna volcanic complex (APVC) of the central Andes [*de Silva*, 1989] (Figure 1). The large (70,000 km^2, 21°S–24°S) APVC lies within the central volcanic zone (CVZ) of the Andean volcanic belt, and is believed to represent the surface

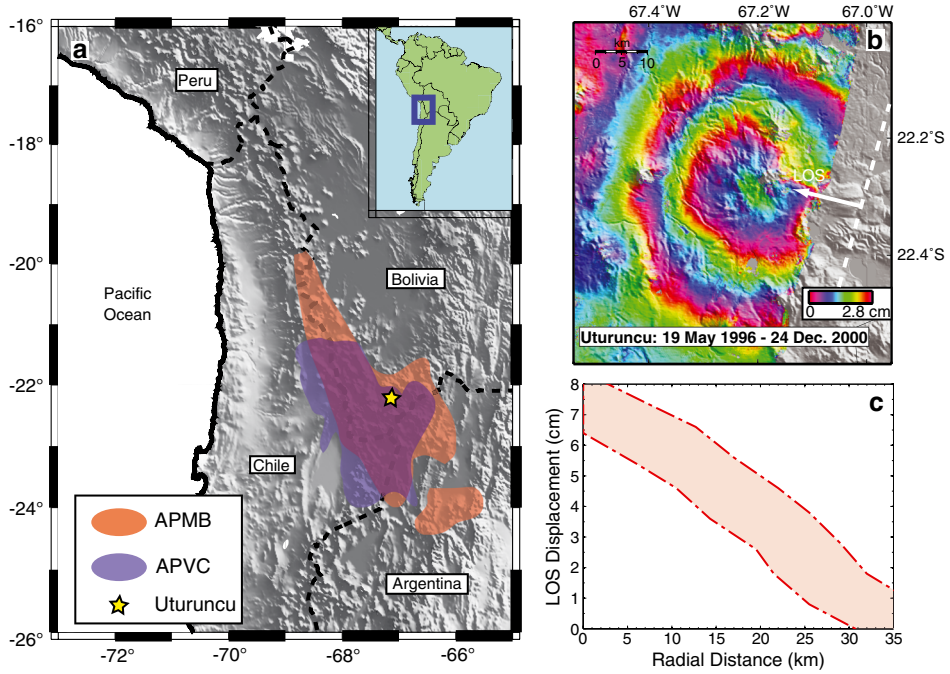

Figure 1. The location and surface deformation of Uturuncu volcano. (a) The Central Volcanic Zone (CVZ) of the Central Andes. Inset shows the location of the CVZ within South America. Location of the APMB and APVC after *Zandt et al*. [2003] and *de Silva et al*. [2006]. (b) Interferogram of Uturuncu volcano showing a concentric, axially symmetric pattern of uplift across a ~70 km wide field. The white arrow shows the satellite look angle. (c) Surface displacement profile extracted from the InSAR image. Data are taken from Figure 1b along a variety of transects to produce a profile representative of the entire image. The broad region is inclusive of the expected uncertainty, an InSAR accuracy of ±1 cm [*Pritchard and Simons*, 2004].

expression of an upper crustal magmatic system, caused by a huge ignimbrite flare-up where at least 15,000 km^3 of magma was erupted between 10 and 1 Ma, creating several large calderas [*de Silva et al*., 2006; *de Silva and Gosnold*, 2007]. Recent research has better constrained the time history of the ignimbrite eruptions using ^{40}Ar/^{39}Ar geochronology to find that the eruptive behavior was episodic and cyclic [*Salisbury et al*., 2011]. Crustal melting, stimulated by an increase in mantle power, is also thought to have contributed to tectonic shortening, resulting in the exceptionally thick (~70 km) crust of the Altiplano region [e.g., *James*, 1971; *Isacks*, 1988; *de Silva*, 1989].

[5] Between 1992 and 2006 a concentric, 70 km wide region around Uturuncu was observed to be deforming at a constant, maximum rate of 1–2 cm/yr in the radar line of sight (LOS) [*Pritchard and Simons*, 2004; *Sparks et al*., 2008]. An anomalously high rate of shallow seismicity was also observed compared to other dormant volcanoes, emanating from a source 3–4 km deep (around sea level) [*Pritchard and Simons*, 2004; *Sparks et al*., 2008; *Jay et al*., 2012]. These are hypothesized to be caused by either brittle deformation of shallow faults within the elastic crust [*Sparks et al*., 2008], the movement of groundwater [*Pritchard and Simons*, 2004], or a combination of the two with stress exerted on a hydrothermal system [*Jay et al*., 2012]. Near-summit active fumaroles at boiling temperature attest to a shallow seated hydrothermal system and a heat source at depth.

[6] The APVC has been related to a magma body constrained from geophysical experiments [*de Silva et al*., 2006; *Schilling et al*., 2006]. The Altiplano-Puna magma body (APMB) is inferred to be a zone of partial melt (~20 vol %), with low density, high electrical conductivity, and low seismic velocity [*Chmielowski et al*., 1999; *Zandt et al*., 2003; *Schilling et al*., 2006]. The presence of the APMB, with its top at roughly 17 km depth, coincides with some of the estimated source depths from previous geodetic modeling attempts, alluding to a magmatic causative source rather than a hydrothermal one [*Pritchard and Simons*, 2004; *Sparks et al*., 2008].

2. Motivation for Study

[7] The observed unrest has warranted a closer study of the causative driving forces. Previous models to explain the surface uplift estimated a source depth between 17 and 30 km, but the inherent assumption of these models was that the constant deformation rate could be reproduced using models of mechanical elasticity [*Pritchard and Simons*, 2004; *Sparks et al*., 2008]. As a result, these models inverted for source parameters that produce instantaneous deformation in an elastic medium. Rocks, however, only behave elastically for very small strains (a few percent or less) at temperatures cooler than the brittle-ductile transition [*Ranalli*, 1995; *Jaeger et al*., 2007]. The geotherm beneath Uturuncu and the APVC is likely perturbed by the presence of the APMB, creating a hot crust with a high heat flow and a shallow brittle-ductile transition zone [*Springer and Forster*, 1998; *de Silva and Gosnold*, 2007; *Jay et al*., 2012], thus inelastic behavior is probable below this level. The likely depth and long-lived (at least 14 years) nature of the causative source are assumed to favor enhanced ductility [*Jaeger et al*., 2007; *Fossen*, 2010]. Therefore, to capture a more realistic rheology and account for time-dependent deformation, we simultaneously solve for source parameters in a mechanically layered viscoelastic medium in addition to homogeneous and heterogeneous elastic mediums, testing a variety of finite source shapes.

[8] By forward modeling using finite element (FE) techniques, this study aims to provide a sensitivity analysis of deformation source characteristics at Uturuncu. Allowing for differing source geometries with mechanically plausible pressure histories we systematically explore the effects of crustal heterogeneity and different rheological behavior to help understand the observed spatial and temporal surface displacement patterns.

3. Methods

3.1. Data

[9] For the purpose of this study, the particular period under investigation is related to the observed uplift between the 19 May 1996 and the 24 December 2000. This period was analyzed in *Pritchard and Simons* [2004] who obtained LOS displacements using C-Band InSAR for a descending orbit of the ERS-2 satellite (Figure 1). Interferograms were processed using the Caltech/JPL software ROI_PAC. The resulting observations have an accuracy of approximately $\pm$1 cm.

[10] We subsampled the interferogram provided to us by Matthew Pritchard (Cornell) along a variety of transects. The relative displacements were extracted against the corresponding distance from the center of maximum deformation and combined to produce a broad region of uplift representative of the entire scene and inclusive of the expected

uncertainty (Figure 1). This was done to complement the axially symmetric model setup and to provide a simpler overview of the deformation, thus facilitating the modeling procedure. Our approach is validated by the observation that the derived deformation pattern is axially symmetric, so profiles from other orientations are almost indistinguishable [*Pritchard and Simons*, 2004, Figures 4J–4L]. The ground deformation profile was then matched to within the observational error by a rigorous forward modeling procedure, systematically exploring the source parameter space (size, shape, depth and pressure). Although a substantial number (>600) of individual models were run to derive a variety of best-fitting source parameter combinations, we acknowledge that as with all forward modeling there is a possibility that another set of combinations could have been missed that also produce valid results.

[11] The axisymmetric models output the computed displacements in radial (U_R) and vertical components (U_Z) so this was converted to match the InSAR LOS (U_{LOS}) [*Hanssen*, 2001] via

$$U_{LOS} = \cos\varphi \sin\theta U_X - \sin\varphi \sin\theta U_Y + \cos\theta U_Z \quad (1)$$

where U_X and U_Y are the displacements in the east-west and north-south components, respectively. The satellite orbit is reflected in the heading (φ) and average incidence (θ) angles, which are 13° and 22°, respectively, in the given interferogram. Given that $U_R = \pm\sqrt{U_X^2 + U_Y^2}$, and approximating the axisymmetric model via an east-west profile on the west side of the volcano where $U_Y = 0$ and $U_R = -U_X$, then equation (1) can be simplified to

$$U_{LOS} = 0.93U_Z - 0.37U_R \quad (2)$$

where a positive U_{LOS} is motion toward the satellite and the negative sign of U_R accounts for a westward horizontal displacement away from the satellite. Henceforth, all model results are presented in the LOS vector for an east-west profile. Models then deemed acceptable are those whose LOS displacement falls entirely within the data plus error bounds described above.

3.2. Model Setup

[12] The structural mechanics module of commercial software COMSOL® Multiphysics, version 4.2a, was used to construct and compute all finite element models (FEMs). The basic axisymmetric FEM setup used is shown in Figure 2, and was adapted according to the suite of models to be run. By utilizing a 200 km × 200 km domain, it is of sufficient size such that the lateral boundary conditions do not affect the results of the interior. To obtain first-order insights on potential source shapes, a selection of widely employed finite geometries are used (spherical, oblate, and prolate spheroids) and the source depths utilized (all given relative to the local elevation) allow the topographic effects to be ignored [*Cayol and Cornet*, 1998].

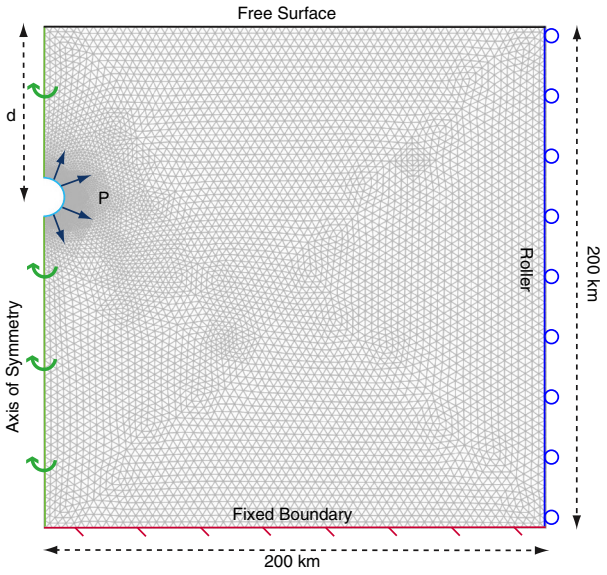

Figure 2. Schematic diagram of the basic FEM setup. *d* is the depth to the center of the source and *P* is the uniform pressure change normal to the boundary of the source, dependent on the model run. The Earth's surface is treated as a free surface, the bottom boundary has a fixed zero-displacement constraint, and the lateral boundary has a roller condition. Mesh and source size are scaled up for illustrative purposes.

[13] Axial symmetry is applied due to the concentric pattern of deformation constrained from InSAR (Figure 1), and transforms the model from two-dimensional into pseudo three-dimensional. It is also cheaper on computing resources, reducing the effective number of elements and therefore speeding up the computational process. Consequently, this also assumes the subsurface structure within the model to be axisymmetric, and therefore continuous across the model diameter. Yet, while there is some evidence of lateral crustal variation in the local Uturuncu region to sea-level depth [*Jay et al.*, 2012], the data are not of sufficient quantity (in terms of depth and lateral extent) to merit inclusion in a more complex and time-consuming fully three-dimensional model. We therefore focus our attentions on large-scale vertical variations in crustal structure across the Altiplano-Puna region, delineated by strong seismic reflectors to ~20 km depth [*Wigger et al.*, 1994; *Zandt et al.*, 2003]. The inclusion of

gravitational body loads did not alter the modeled deformation results and are therefore excluded from further discussion. Additionally, given the concentric pattern of the observed ground deformation, dipping sources were not considered in the FE analysis.

3.3. Model Physics

3.3.1. Elasticity

[14] The first suite of models was based on the assumption of linear elasticity throughout the entire model domain. This implies: (1) stress is directly proportional to strain via Hooke's Law, (2) instantaneous deformation upon application of the load, (3) 100% recoverable deformation upon removal of the load, and (4) that all this happens using a load below the yield limit of the material [e.g., *Ranalli*, 1995].

[15] The elastic models require two independent material properties. A constant value of 0.3 was chosen for the Poisson's Ratio (ν) in both the homogeneous and heterogeneous (Ho and He, see Table 1) models, representative of an andesitic crust [e.g., *Gercek*, 2007; *Sparks et al*., 2008]. Tests that applied a varying Poisson's ratio with depth had only a very minor effect on the uplift patterns, inducing a slight narrowing and decreasing the pressure requirement by ~5%, and are thus excluded to prevent an overparameterization of model fits.

[16] Instead, more focus is placed on the choice of Young's modulus, representative of the stiffness of the medium, and directly influencing the amount of strain produced for a given stress (via Hooke's Law). For the homogeneous model domain, the Young's modulus (E) was calculated using Poisson's ratio (ν), density (ρ), P-wave velocity (V_P), and the P-wave modulus (M) using the following sequence of empirical relations [*Brocher*, 2005]:

$$\rho = 1.6612V_P - 0.4721{V_P}^2 + 0.067\,{V_P}^3 - 0.0043{V_P}^4 + 0.000106{V_P}^5 \quad (3)$$

$$M = {V_P}^2 \cdot \rho \quad (4)$$

$$E = \frac{M(1+\nu)(1-2\nu)}{(1-\nu)} \quad (5)$$

[17] The input value of V_P was taken from seismic receiver functions of the nearest published seismic section at 21°S, which found an average P-wave velocity of 6 km/s in the Altiplano region [*Wigger et al*., 1994]. The resultant Young's modulus of 84.2 GPa is consistent with values found in volcanic regions [*Gudmundsson*, 2011].

Table 1. List of Subsurface and Source Parameters

Variable	Definition	Dimensions
Subsurface Parameters		
ν	Poisson's ratio	–
E	Young's modulus	Pa
G	Shear modulus (rigidity)	Pa
μ	Fractional shear moduli	–
η	Viscosity	Pa s
τ	Relaxation time	s
T_0	Tensile strength	Pa
K_C	Fracture toughness	Pa $m^{½}$
Model Names		
Ho	Homogeneous domain	–
He	Heterogeneous domain	–
SS	Spherical source	–
PS	Prolate source	–
OS	Oblate source	–
[Number]	Relates to size and depth	–
Source Characteristics		
a	Semimajor axis (vertical)	m
b	Semiminor axes (horizontal)	m
α	Radius of a SS	m
d	Depth	m

[18] However, evidence of vertical variations in the crustal structure of the central Andes, and the presence of a low-velocity zone inferred to be a region of partial melt (the APMB) warranted the use of an additional set of models incorporating a heterogeneous computational domain [*Wigger et al*., 1994; *Schmitz et al*., 1997; *Chmielowski et al*., 1999; *Yuan et al*., 2000]. Using results from *Wigger et al*. [1994], and two computed velocity models [*Leidig and Zandt*, 2003], a layered, heterogeneous crustal medium was constructed using six individual homogeneous blocks (Figure 3). Corresponding P-wave velocities were extracted from the published data and used to calculate density and then Young's modulus using equations (3)–(5) (see Table 2 for layer depths and calculated values). As with the homogeneous domain, a Poisson's ratio of 0.3 was still maintained throughout each layer.

[19] To ensure the elastic models were correctly setup, benchmark models were run to compare to the analytical solution of a "Mogi" source [*Mogi*, 1958], utilizing the necessary homogeneous, isotropic, elastic half-space assumptions. For the same given deformation source and elastic medium, and an FEM domain consisting of ~60,000 elements, the analytical and FE results are more than 99% in agreement, indicating that the benchmark FEM is correctly setup and can thus be applied to more informative problems. Very slight mismatches are thought to be artifacts of the mesh density, with the

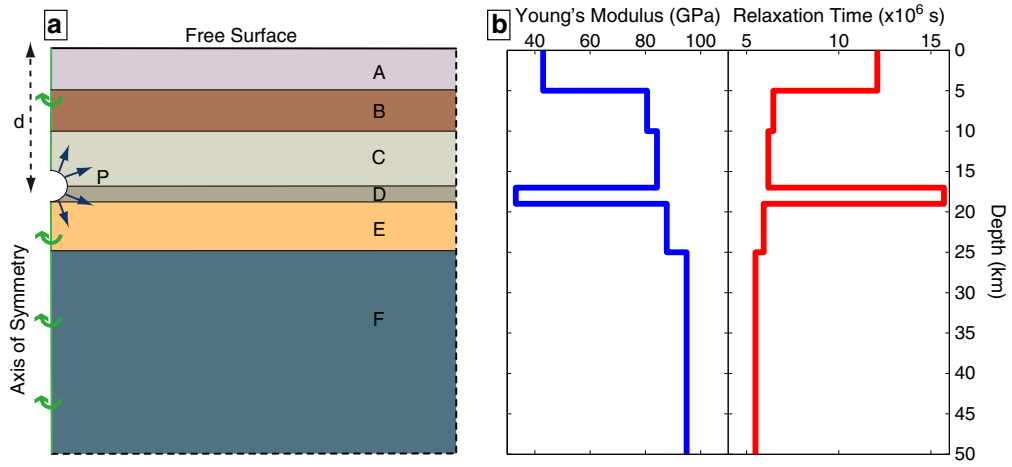

Figure 3. (a) The layered FEM setup employed in the heterogeneous elastic and viscoelastic models. The setup is the same as in the Figure 2, but with the uniform subsurface replaced with a layered structure. Letters A–F indicate the different layers, and each layer boundary is free to deform. Only a selection of the entire model domain is shown. (b) The layer properties used in the heterogeneous elastic and viscoelastic models. Young's modulus and relaxation time (viscoelastic models only) are displayed as a function of depth, calculated as described in the text.

Table 2. Layer Properties for the Heterogeneous Models (Elastic and Viscoelastic)

Layer	Depth (km)	V_P (km/s)	Density (g/cm^3)	E (GPa)	ν	G (GPa)	τ (×10^{6}s)
A	0–5	4.5	2.45	43.0	0.3	16.5	–
B	5–10	5.9	2.67	80.6	0.3	31.0	6.45
C	10–17	6.0	2.70	84.2	0.3	32.4	6.18
D	17–19	4.0	2.39	33.1	0.3	12.7	15.71
E	19–25	6.1	2.72	87.7	0.3	33.7	5.93
F	25–50	6.3	2.76	94.9	0.3	36.5	5.48

FE solution underestimating the vertical and horizontal displacement by 0.2% and 0.7% respectively in the far-field. The advantages of increasing the mesh density to further improve the goodness of fit are far outweighed by the increased computational cost that would be required to run the models.

3.3.2. Viscoelasticity

[20] Building on the homogeneous and heterogeneous elastic models described above, efforts to further investigate causative source processes and time-dependent deformation while considering an anelastic crustal rheology were obtained by first-order approximations of subsurface viscoelasticity. This was implemented using a standard linear solid model, which combines viscous and elastic elements in parallel and series (Figure 4), and allows for an instantaneous elastic deformation followed by a time-dependent viscous creep [*Fung*, 1965; *Christensen*, 2003]. Its characteristic relaxation time, τ, is defined as

$$\tau \approx {}^{\eta}/_{G \cdot \mu_1} \quad (6)$$

where η is the viscosity, G is the total shear modulus (rigidity) and μ_1 is the fractional shear moduli in the Maxwell arm [*Del Negro et al.*, 2009]. The values used in this study were $\eta = 10^{17}$ Pa s,

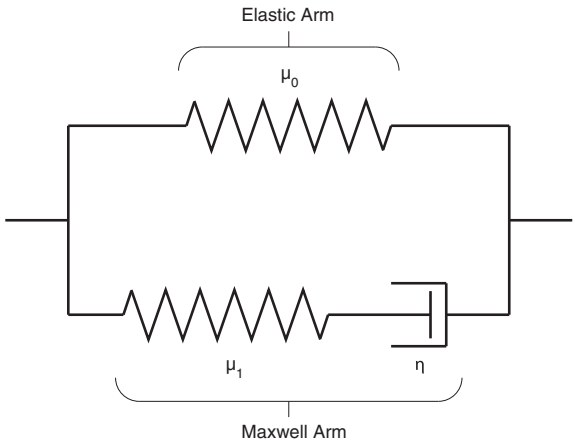

Figure 4. The standard linear solid viscoelastic model. The rigidity (G) of each viscoelastic layer in Figure 3 is split across the elastic and Maxwell arms according to the values of the two fractional shear moduli and $\mu_0 + \mu_1 = 1$. The value of viscosity, η, is 10^{17} Pa s.

and $\mu_1 = 0.5$ (splitting the total rigidity equally between the two elastic components). These were kept constant to reduce the number of variables in the model setup and hence focus the efforts of the current study on processes related to the nature of the causative source rather than the rheology of the crust. However, a subset of models that tested the sensitivity of these values demonstrated that an increase in μ_1 (or decrease in μ_0) causes a greater proportion of creep, trending toward near limitless creep when $\mu_1 = 1$, an unrealistic scenario for the Earth's crust (Figure 4). Conversely, increasing η produces a proportional increase in τ and less displacement for the same given pressure and time interval.

[21] The viscoelastic representation was realized in the FEMs by modeling layers B–F (Figure 3 and Table 2) as viscoelastic but keeping the top A layer (5 km thick) as elastic, synonymous with evidence of shallow seismicity and estimates of a shallow brittle-ductile transition [*Jay et al*., 2012]. Each layer then had its own relaxation time according to equation (6) and its value of rigidity derived from the Young's modulus via $G = E/2(1 + v)$. This viscoelastic setup was successfully benchmarked against the equivalent analytical model using a full viscoelastic half-space and a spherical source [*Del Negro et al*., 2009].

4. Results and Discussion

4.1. Elastic Models

[22] Despite the crust beneath Uturuncu being particularly hot and likely breaching the assumptions of linear elasticity (as described above), the initial elastic models are useful to provide constraints as to the possible shape, size, and depth of the causative source, as well as to assess the sensitivities to crustal heterogeneity compared to homogeneity assumed in most previous models. These results can then guide more realistic, anelastic models that better explain the likely subsurface conditions producing the observed spatial and temporal uplift patterns.

4.1.1. Source Shape and Depth

[23] The large uplift footprint at Uturuncu (~70 km wide) requires a deep source to reproduce the same spatial extent as that observed through InSAR. From over 600 individual models constructed during this investigation (Table 3), we find the range of acceptable depths for the causative source between 18 and 35 km below the surface (assuming a layered crust). This is similar to the findings of *Pritchard and Simons* [2004] who found a range of 17–30 km using an analytical inversion technique.

[24] Depending on the shape of the source, the specific depth range changes, such is the nonuniqueness of the problem when using a data set with only one dimension of observed deformation [*Dieterich and Decker*, 1975]. This is because different shapes produce relatively more vertical or radial displacement. An increasingly oblate source produces a narrower, more "peaked" displacement pattern, with the magnitude of deformation falling rapidly with radial distance (Figure 5). Such patterns exist due to the amount of surface area of the source that faces vertically upward. An oblate source, having a slightly flattened top, presents a larger surface than a more pointed, prolate source. Consequently, more displacement is transferred directly upward in the case of the oblate source, resulting in the peaked displacement pattern. Therefore, in order to dissipate the peaked pattern and better fit the broad observed surface displacement, the oblate sources require situating at greater depths (30–35 km) than the prolate sources (18–25 km). Spherical sources are in between the two (28–33 km).

[25] The prolate source depth range coincides with strong evidence of partial melt. Yet, while the APMB has been seismically modeled as a thin layer, the bottom is poorly constrained and alternative models with a thicker zone of partial melt cannot be rejected [e.g., *Chmielowski et al*., 1999; *Schilling et al*., 2006]. Hence, the oblate and spherical source depth ranges could also coincide with a magma storage region.

4.1.2. Source Size vs. Pressure Change

[26] Because our elastic models do not account for the subsurface state of stress (it is assumed lithostatic), we take the assumption that the tensile strength of host rock is the utmost value that a magma chamber can sustain before rupturing and triggering the emplacement of a dyke [*Gudmundsson*, 1990, 2006], and can hence estimate a maximum value

Table 3. The Range of Source Parameters Explored in All Models of This Study

Source Parameter Ranges	Source Shape		
	Prolate	Spherical	Oblate
Depth (km)	16–25	16–35	16–35
Semimajor axis (km)	1.0–10.0	0.5–8.5	0.9–8.0
Semiminor axis (km)	0.5–5.6	0.5–8.5	1.5–12.0
P (MPa)	2.91–5200	1.75–11500	1.19–420

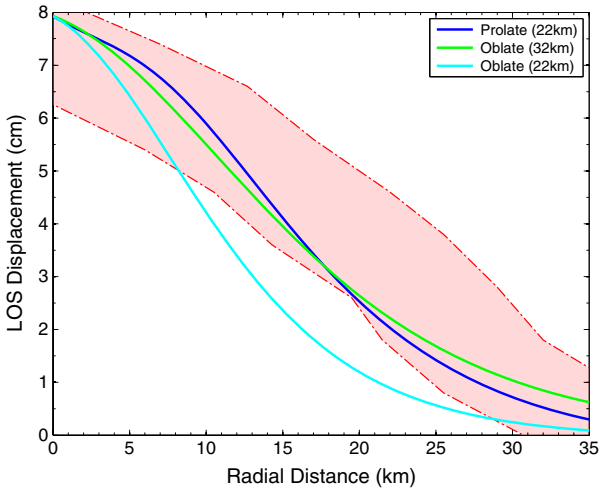

Figure 5. The trade-off between source shape and depth. Due to the different relative amounts of vertical and radial displacement generated for different source shapes, they require situating at different depths to match the InSAR signal. The oblate sources produce a narrower or "peaked" surface uplift pattern that must be dissipated by locating them at greater depths than the prolate sources. Source dimensions for the oblate source are $a = 3$ km and $b = 6.5$ km with pressures of 5.0 and 13.1 MPa for the 22 and 32 km depths, respectively. The prolate source has $a = 10$ km and $b = 3.5$ km with a pressure of 21.0 MPa.

for the source pressure in the elastic models. Most dykes propagate as mode I extension fractures [*Gudmundsson*, 2002] and there exists an empirical relationship between the tensile strength of rock (T_0) and mode I fracture toughness (K_C), where T_0 $6.88K_C$ [*Zhang*, 2002]. Using andesitic values for K_C, which increase from 2.5 ± 0.5 MPa $m^{1/2}$ to 3.5 ± 1 MPa $m^{1/2}$ at magmatic temperatures [*Smith et al.*, 2009], T_0 varies from 14 to 31 MPa. Applying an upper limit of 31 MPa as a threshold value, all elastic models with pressure requirements exceeding this were discarded as being mechanically unfeasible.

[27] Building upon previous work, initial model runs were conducted using similar, small source sizes, e.g., a prolate source with a semimajor axis of 1 km [*Pritchard and Simons*, 2004]. However, the required pressures to reproduce the maximum observed uplift were on the order of hundreds of MPa to several GPa, and thus rejected as being highly unrealistic. For the specific case of a prolate source centered at 17 km depth where $a = 1$ km and $b = 0.67$ km (a is the semimajor axis, b is the semiminor axis) the necessary pressures are 3.8 GPa and 1.7 GPa for the homogeneous and heterogeneous mediums, respectively, 50 to 100 times greater than the inferred upper limit of pressurization.

[28] Subsequent models were run using much larger source sizes in order to achieve the correct magnitude of uplift for an acceptable pressure value. This meant a semimajor axis of 8–10 km for the prolate sources and semiminor axes of 10–12 km for the oblate sources (Table 4).

4.1.3. Effect of Mechanical Weakness

[29] The modeled low-velocity zone of this study (layer D in Figure 3 and Table 2) with a Young's modulus of 33.1 GPa is particularly soft when compared to its surroundings. Consequently, the pressurized sources preferentially deform into this layer if placed at a coincident depth, thus altering the resultant surface displacement, as evidenced by the comparison of models HePS117 and HoPS117 (Figure 6). Both models match the maximum deformation, but HePS117 has a significantly narrower displacement pattern that better matches the entire InSAR profile. This is due to the distortion of the subsurface deformation by the elastic layering; more of the source-region deformation is focused into the softer layer (Figure 6), meaning less displacement is transferred to the surface. The source depth soft layer effectively acts to buffer the surface deformation.

[30] The heterogeneous model also requires a smaller and more mechanically acceptable pressure change (28.1 MPa) to replicate the maximum uplift, for the same source geometry and depth as the homogeneous medium (56.5 MPa). Such patterns

Table 4. Acceptable Modeled Source Parameter Ranges and Mean Source Parameters Used in the Viscoelastic Models

	Prolate		Oblate		Spherical	
Acceptable source parameter Ranges	Depth (km)	18–25	Depth (km)	30–35	Depth (km)	28–33
	Semimajor axis (km)	8–10	Semimajor axis (km)	1–3	Radius (km)	5–7
	Semiminor axes (km)	3–3.5	Semiminor axes (km)	10–12		
Mean source parameters	Depth (km)	20.6	Depth (km)	32.8	Depth (km)	30.4
	Semimajor axis (km)	9.2	Semimajor axis (km)	2.0	Radius (km)	6.1
	Semiminor axes (km)	3.1	Semiminor axes (km)	10.6	Volume (km^3)	950
	Volume (km^3)	370	Volume (km^3)	941		

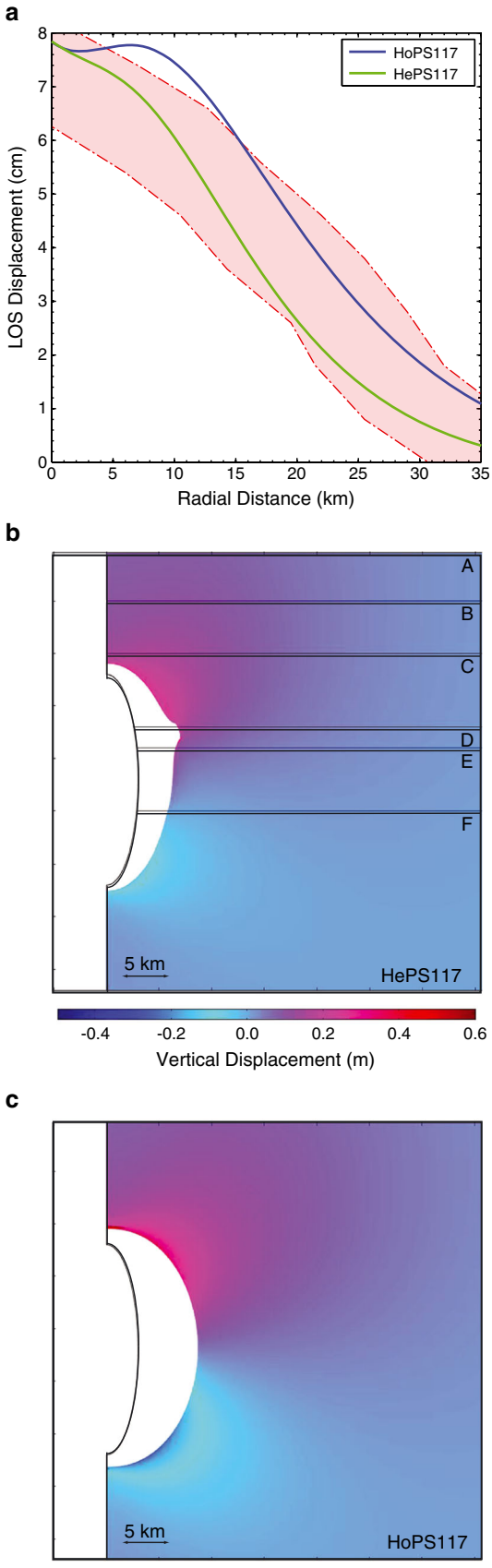
a
HoPS117
HePS117
LOS Displacement (cm)
Radial Distance (km)
b
A
B
C
D
E
F
5 km
HePS117
-0.4
-0.2
0.0
0.2
0.4
0.6
Vertical Displacement (m)
c
5 km
HoPS117

Figure 6

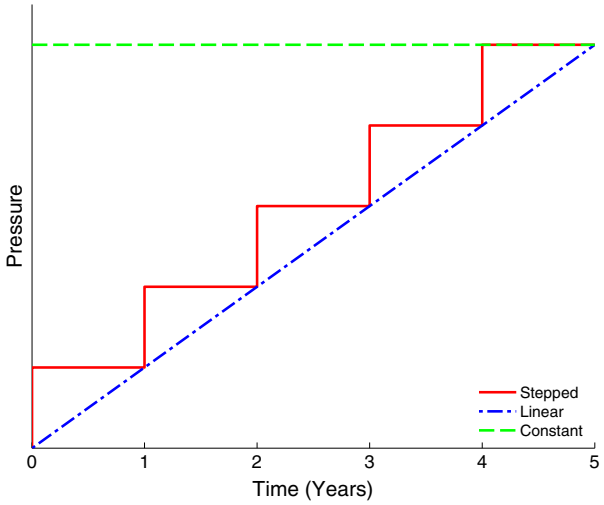

Figure 7. Pressure functions used in the viscoelastic models.

are found in all models comparing homogeneous and heterogeneous domains. This is the combined result of softer layers above and around the source amplifying the deformation when compared to a uniform subsurface with a stiffer average Young's modulus. These findings agree with other studies in that homogeneous models often necessitate highly unrealistic pressure changes when compared to a heterogeneous setup [*Manconi et al.*, 2007; *Geyer and Gottsmann*, 2010; *Hautmann et al.*, 2010].

4.1.4. Limitations of Mechanical Elasticity

[31] The heterogeneous media derived and implemented in this study were not designed to replicate the exact crustal structure of the Altiplano-Puna region, but to provide viable approximations on the effect mechanical heterogeneities can have on deformation predictions. A more accurate representation would only be possible if the true subsurface elastic (Young's modulus and Poisson's ratio) constants were known in situ to significant depths. For the given setup, an obvious drawback of the elastic models is that the deformation is instantaneously reproducing the observations from InSAR that were built up over 5 years. It appears that the maximum LOS deformation rate has been roughly constant through time at 1–2 cm/yr for at least 14 years [*Sparks et al.*, 2008], and this temporal deformation pattern is not possible to reproduce with elastic models without including a time-dependent pressure condition. We can also more realistically assume that the mechanical behavior of the crust is inelastic below 5 km depth [e.g., *Jay et al.*, 2012]. We therefore invoke viscoelastic behavior for the crust in a separate set of models to account for this rheology and the time-dependent deformation.

Table 5. Comparison of Elastic and Viscoelastic Modeled Pressure Functions

Source	Constant P (MPa)		Time-Dependent P (MPa/yr)[a]
Shape	Elastic	Viscoelastic	Stepped and Linear
Prolate	25.1	15.0	3.00
Oblate	2.9	1.7	0.33
Spherical	13.5	8.1	1.60

[a]The time-dependent pressures were only applied to the viscoelastic models.

[32] The elastic model results are thus used to serve as an indicator as to the source shape, depth, and size. For the three source shapes, all heterogeneous elastic models that fit the data within error and with an acceptable pressure requirement (≤ 31 MPa, as a proxy for source size) are grouped and averaged to produce a representative source for each shape (Table 4). These representative sources are then used in the viscoelastic models, because the final shape of the surface uplift profile will be the same as the elastic models, but with a different time-history to get there.

4.2. Viscoelastic Models

[33] The viscoelastic models include a time-dependent factor by accounting for viscous creep following an instantaneous elastic deformation. The size of the initial elastic deformation is dependent on the magni-

Figure 6. A comparison of the effect of homogeneity versus heterogeneity for the same prolate source geometry and depth. (a) Surface displacement profiles. A heterogeneous medium alters the surface displacement pattern due to the combined influence of stiff and soft layers and requires a smaller, more realistic pressure to produce the same magnitude of uplift. (b and c) The effect of a source depth soft layer on the deformation of a source. Both panels show the same source, embedded in the heterogeneous medium (Figure 6b) and the homogeneous medium (Figure 6c). Colors relate to the vertical displacement (as per the shared colorbar), and the white shape shows the exaggerated outline of the deformed source after the pressure is applied. In the heterogeneous medium the source preferentially deforms into the softer layer (D), compared to the homogeneous medium, which exhibits a concentric deformation pattern. This in turn affects the displacement pattern produced at the surface (Figure 6a) as the soft layer buffers the subsurface deformation. Letters A–F correspond to the layers in Figure 3 and Table 2. Source geometry: $a = 10$ km, $b = 3$ km, and $d = 22$ km.

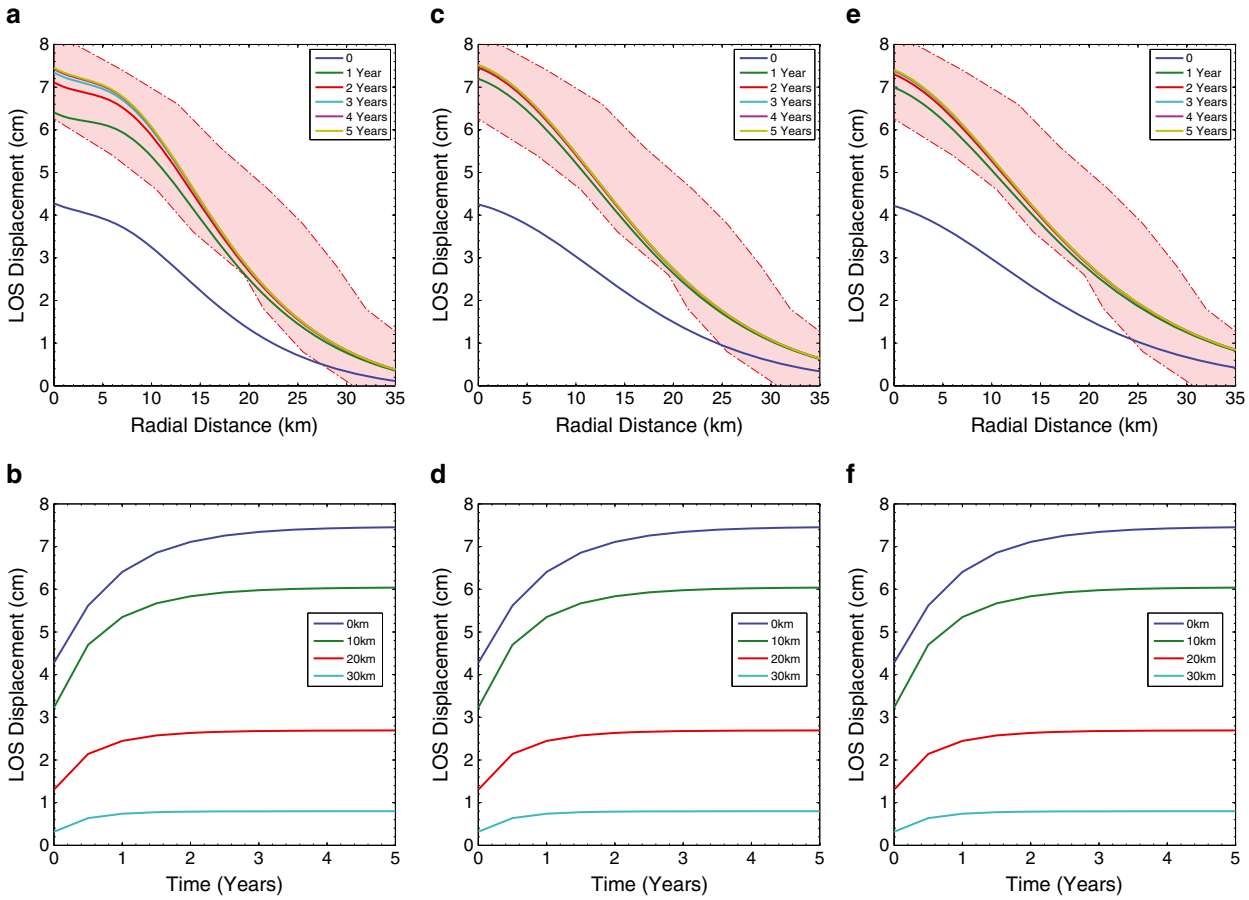

Figure 8. Constant pressure viscoelastic model results. Displacement is shown against distance (top) and cumulatively against time (bottom) for a representative prolate (a and b), oblate (c and d), and spherical (e and f) source. None of the models produce a constant uplift rate as the displacement plateaus after approximately 1 year. Model geometries are as displayed in the bottom half of Table 4.

tude of the pressure applied to the source, while the amount of time-dependent creep is controlled by the viscosity and fractional shear moduli in the Maxwell arm of the standard linear solid model.

4.2.1. Constant Source Pressure

[34] As with the elastic models, the first set of viscoelastic models were run with a constant source pressure throughout the computation (Figure 7). The pressure required to match the spatial deformation pattern after 5 years is 40% smaller than the pressure requirement in the equivalent elastic model (Table 5). However, the temporal deformation pattern is still not met (Figure 8). This is because the maximum deformation (when the amount of viscous creep has reached its limit) is attained after approximately 1 year. Therefore, if the initial pressure is large enough such that after a year's worth of creep the spatial deformation is matching that of the InSAR, the initial elastic response is exaggerated. The deformation rate is then at a maximum (~4 cm/yr) at the start of the simulation and subsequently decreases to zero. Hence, in order to recreate the constant uplift rate that is observed, the source pressure must increase incrementally as the viscous component of the deformation plateaus.

4.2.2. Time-Dependent Source Pressure

[35] Motivated by the failure of the constant source pressure models, a time-dependent pressure is introduced. To mimic an incremental (yearly, for lack of better constraints from observations) increase in the source pressure, a step function is used (Figure 7). This means that as the viscous component of the deformation approaches its limit (and the total deformation would plateau for a given pressure), the pressure is increased and the cycle repeats itself. The pressure increase at each step is then considerably smaller than that required in the constant pressure models, meaning the first initial pressure produces an uplift rate that is commensurate with the one recorded at Uturuncu and remains quasi-

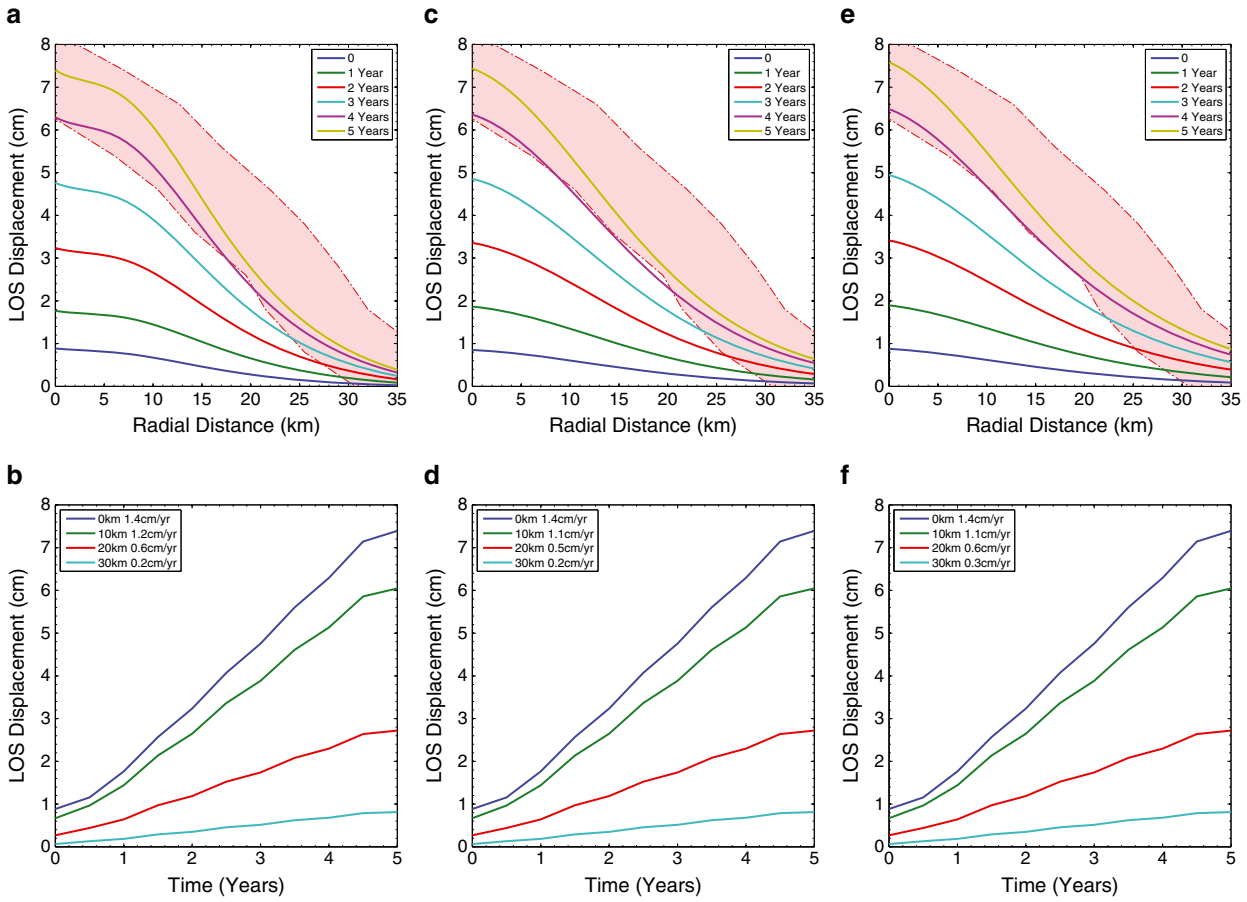

Figure 9. Stepped pressure viscoelastic model results. Displacement is shown against distance (top) and cumulatively against time (bottom) for a representative prolate (a and b), oblate (c and d), and spherical (e and f) source. All models produce constant uplift rates that match the observations made at Uturuncu since 1992, as well as recreating the spatial deformation pattern from the 5 year period forming the focus of this study. Model geometries are as displayed in the bottom half of Table 4.

constant throughout the model run. The resulting uplift then matches both the spatial and temporal patterns for all source shapes and these are our preferred models (Figure 9). This demonstrates how a pressure-time function may play a first-order role in explaining the temporal deformation pattern.

[36] In addition to a step function, a linearly increasing pressure function (Figure 7) can also be used to match both the spatial and temporal deformation. The uplift patterns and rates are extremely similar to those of the step function but with smoother gradients. In either case, the results allude to a continual increase in the pressure driving the magmatic system and causing surface uplift.

5. Implications for the Magmatic System

[37] All three source-shapes can produce displacement profiles to match that of the InSAR due to the inherent nonuniqueness of the problem, and a lack of observational geodetic data from more than one component of the deformation field. All can then be related to the pressurization of magma associated with the APMB. In the case of the prolate source, this may imply that a causative body protruding or rising out from the top of the APMB is causing the surface uplift. The fact that ground displacement patterns are dominantly controlled by stresses generated along the upper surface of finite pressure sources may provide additional support for this inference [*Yun et al.*, 2006]. On the other hand, where the spherical and oblate sources are used, this alludes to pressurization within the APMB as the cause (Figure 10). Such pressurization within (or below) the APMB appears unlikely given the available constraints from geophysical data on the partially molten anomalous body. Relaxation of stresses over time would likely make this mechanism unsustainable. Therefore, from the suite of models presented, we prefer a model of a prolate source extending from the APMB upward.

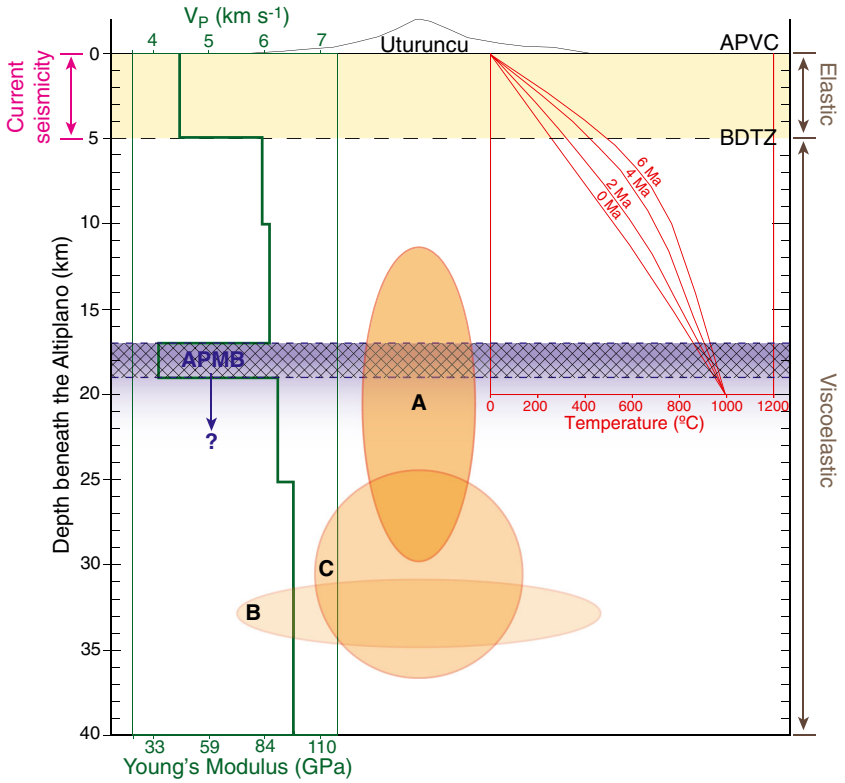

Figure 10. Cross-section through the crust beneath Uturuncu. A, B, and C show the representative prolate, oblate, and spherical sources respectively. In the case of the prolate shape, the deformation source is seen to rise out of the APMB and this is our preferred model. Pressurization of the deeper oblate and spherical sources within or below the APMB is likely unsustainable due to the relaxation of stresses over time. The seismic velocity profile is constrained from the literature (as described in the text), current seismicity and brittle-ductile transition zone after *Jay et al*. [2012], and the temperature profiles after *de Silva and Gosnold* [2007] for a range of years following the intrusion of the APMB beneath the APVC.

[38] In a recent paper, *Fialko and Pearse* [2012] proposed a rising magmatic diapir as the source of ground deformation at Uturuncu. While our preferred model does deviate from theirs, both models allude to an anomalous body extending from the APMB upward causing the broad deformation anomaly. This is emphasized by a final viscoelastic model that replaces the source cavity with a half-prolate shape protruding from the APMB (Figure 11). The shape is taken from the top half of the preferred prolate source model and we apply a stepwise increasing pressure function along its outer boundary (as in Figure 7), equivalent to 1.2 MPa/yr. This produces a deformation pattern that matches the spatial and temporal observations at Uturuncu, with a constant, maximum uplift rate of 1.4 cm/yr.

[39] The pressure condition we apply to the boundaries of the modeled sources may arise from the replenishment of the magma chamber. However, the increasing pressure histories required to match the temporal and spatial deformation patterns preclude the arrival of dykes in swarms, in favor of the continuous or rhythmic arrival of magma. An alternative explanation for the required pressure history is if the pressure is caused by buoyancy of the source; the rise of the head of the magma body as a ballooning diapir could cause the observed ground deformation pattern without the need for constant replenishment from depth [*Diez et al*., 2011; *Fialko and Pearse*, 2012]. This would only be possible if a thermally matured overlying crust allowed creep flow.

[40] To further constrain the causative source parameters, the full three-dimensional displacement field is required. This could be incorporated into a fully three-dimensional FEM, with vertical and lateral variations in subsurface properties, to deduce more accurate source characteristics. There is also scope to assess other inelastic rheologies, such as visco-plastic and power-law viscoelastic, to see how these could influence the inferred source processes and parameters. Additionally, geodetic surveys are often complemented with other geophysical techniques that provide supplementary data about the observed anomaly. Useful accompaniments are gravity surveys, which can identify subsurface mass changes and infer density distributions [*Gottsmann et al*.,

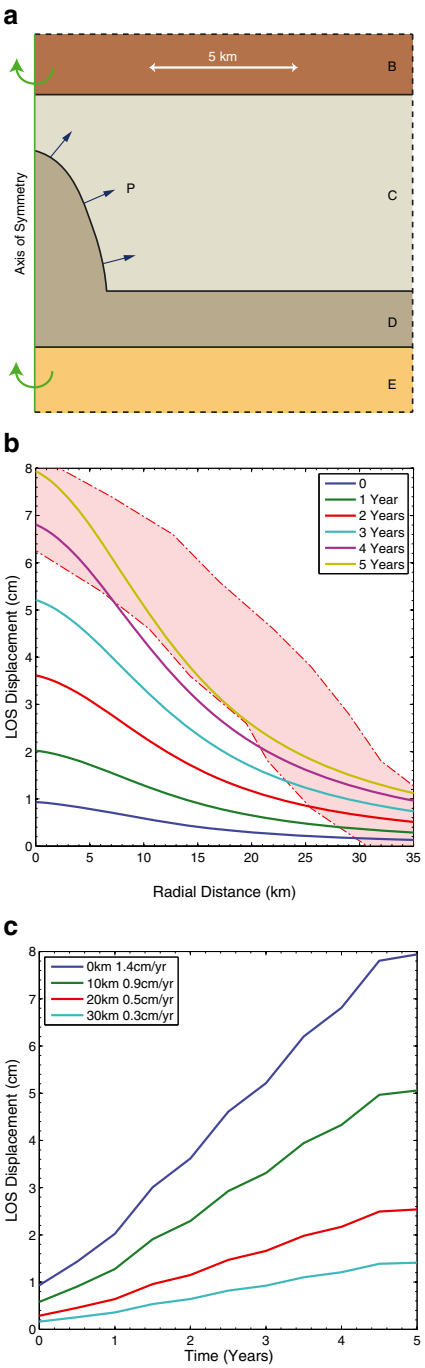

Figure 11. Viscoelastic protrusion model. (a) The FEM setup. The source cavity is replaced with a body extending from the APMB (layer D), and a pressure condition (*P*) is applied along its boundary. Letters B–E indicate the different layers (Figure 3 and Table 2) while only a selection of the entire model domain is shown. (b) Displacement results against distance for the 5 year study period show how the model matches the spatial uplift pattern. (c) Cumulative displacement results against time display a constant deformation rate that varies from 1.4 cm/yr directly above the source to 0.3 cm/yr at 30 km radial distance, thus matching the observed temporal deformation rate.

2008; *Currenti et al.*, 2007]. The latter should be able to image bodies of anomalous density in or around the postulated source regions and possibly distinguish between the different idealized source shapes [*del Potro et al.*, 2011]. Therefore, while the current models provide sensitivity analyses and first approximations of crustal mechanics and causative source characteristics (using the currently available data), more work is underway to account for the additional complexities mentioned above.

6. Conclusions

[41] We explored a variety of source parameters and crustal representations to better understand the processes causing the observed spatial and temporal surface uplift patterns at Uturuncu volcano. Investigating elastic heterogeneity compared to homogeneity with a layered crustal structure demonstrated the measurable affect such differences can have on the resultant deformation pattern. In particular, the presence of a source depth soft layer severely altered surface displacement patterns. Source-scale examinations showed that the irregular deformation of the expanding source, caused by preferential intrusion into the softer layer, manifested itself in the surface displacement pattern. Also, softer layers above a source in a heterogeneous medium were found to amplify the observed surface displacement when compared to a homogeneous medium.

[42] The elastic models were useful to provide constraints as to the possible shape, size, and depth of the causative source, and to assess the sensitivities to crustal heterogeneity compared to homogeneity. The oblate sources required centers situated at greater depths (30–35 km) than the prolate sources (18–25 km) to produce the correct spatial deformation, while a mechanically and geologically plausible pressure estimate necessitated a semimajor axis of 8–10 km for the prolate sources and semiminor axes of 10–12 km for the oblate sources. The spherical sources were located at 28–33 km depth with radii of 5–7 km. However, the elastic models could only fit the spatial deformation pattern without any insights into the temporal pattern.

[43] We therefore examined a set of viscoelastic models to account for the time-dependent deformation, and also to satisfy the rheology of the subsurface in this region, which is assumed to be anelastic. With a constant pressure, the viscoelastic models required a 40% smaller pressure than the equivalent elastic model to match the spatial deformation pattern after 5 years, but the temporal deformation

pattern was still not met. An incremental increase in source pressure produced an uplift rate that is commensurate with the one recorded at Uturuncu and remained quasi-constant throughout the model run. The resulting uplift then matched both the spatial and temporal patterns for all source shapes, thus demonstrating how a pressure-time function may play a first order role in explaining the temporal deformation pattern.

[44] Our preferred model suggests that pressurization of a magma source extending upward from the APMB is causing the observed surface uplift and alludes to a continued increase in this pressure to explain both the spatial and temporal patterns. Placing this study in a broader context it is clear that efforts to better understand the source dynamics and characteristics beneath the Altiplano-Puna region will aid in the long-term categorization of Uturuncu's level of unrest and hazard assessment. Key to this is how the assumed pressurization of the APMB derived source could relate to potential eruptive, or even caldera-forming activity.

Acknowledgments

[45] This work was supported by the Natural Environmental Research Council (grant NE/G01843X/1), the European Union Framework Program 7 (grant 282759, "VUELCO") and the Royal Society (University Research Fellowship). We thank Matthew Pritchard, Ciro Del Negro and editor James Tyburczy for their constructive reviews.

References

Anderson, E. M. (1936), The Dynamics of the Formation of Cone Sheets, Ring dykes, and Caldron subsidences, *Proc. Roy. Soc. Edinburgh*, *56*(3-4), 128–157.

Brocher, T. A. (2005), Empirical relations between elastic wavespeeds and density in the earth's crust, *Bull. Seismol. Soc. Am.*, *95*(6), 2081–2092.

Cayol, V., and F. H. Cornet (1998), Effects of topography on the interpretation of the deformation field of prominent volcanoes - Application to Etna, *Geophys. Res. Lett.*, *25*(11), 1979–1982.

Chmielowski, J., G. Zandt, and C. Haberland (1999), The central Andean Altiplano-Puna magma body, *Geophys. Res. Lett.*, *26*(6), 783–786.

Christensen, R. M. (2003), *Theory of Viscoelasticity: An Introduction*, Dover Publications, New York.

Currenti, G., C. Del Negro, and G. Ganci (2007), Modelling of ground deformation and gravity fields using finite element method: an application to Etna volcano, *Geophys. J. Int.*, *169*(2), 775–786.

Currenti, G., A. Bonaccorso, C. Del Negro, D. Scandura, and E. Boschi (2010), Elasto-plastic modeling of volcano ground deformation, *Earth and Planetary Science Letters*, *296*(3-4), 311–318.

Davis, P. M. (1986), Surface deformation due to inflation of an arbitrarily oriented triaxial ellipsoidal cavity in an elastic half-space, with reference to Kilauea Volcano, Hawaii, *J. Geophys. Res.*, *91*, 7429–7438.

Del Negro, C., G. Currenti, and D. Scandura (2009), Temperature-dependent viscoelastic modeling of ground deformation: Application to Etna volcano during the 1993-1997 inflation period, *Physics of the Earth and Planetary Interiors*, *172*, 299–309.

del Potro, R., M. Diez, J. Gottsmann, A. Camacho, and M. Sunagua (2011), Gravimetric imaging of partially molten bodies beneath the Bolivian Altiplano, *abstract S31B-2237 presented at AGU Fall Meeting 2011*, San Francisco, United States of America.

de Silva, S. L. (1989), Altiplano-Puna volcanic complex of the central Andes, *Geology*, *17*(12), 1102–1106.

de Silva, S. L., G. Zandt, R. Trumbull, J. G. Viramonte, G. Salas, and N. Jimenez (2006), Large ignimbrite eruptions and volcano-tectonic depressions in the Central Andes: a thermomechanical perspective, *Geological Society, London, Special Publications*, *269*, 47–63.

de Silva, S. L., and W. D. Gosnold (2007), Episodic construction of batholiths: Insights from the spatiotemporal development of an ignimbrite flare-up, *J. Volcanol. Geotherm. Res.*, *167*(1-4), 320–335.

Dieterich, J. H., and R. W. Decker (1975), Finite-element modeling of surface deformation associated with volcanism, *J. Geophys. Res.*, *80*(29), 4094–4102.

Diez, M., R. del Potro, and J. Gottsmann (2011), Mechanics of magma ascent beneath the Altiplano-Puna volcanic complex, Central Andes, Bolivia: igneous diapirism through the upper crust, *abstract V33C-2669 presented at AGU Fall Meeting 2011*, San Francisco, United States of America.

Dragoni, M., and C. Magnanensi (1989), Displacement and stress produced by a pressurized, spherical magma chamber, surrounded by a viscoelastic shell, *Physics of the Earth and Planetary Interiors*, *56*(3-4), 316–328.

Dvorak, J. J., and D. Dzurisin (1997), Volcano geodesy: The search for magma reservoirs and the formation of eruptive vents, *Reviews of Geophysics*, *35*(3), 343–384.

Fialko, Y., Y. Khazan, and M. Simons (2001), Deformation due to a pressurized horizontal circular crack in an elastic half-space, with applications to volcano geodesy, *Geophys. J. Int.*, *146*(1), 181–190.

Fialko, Y., and J. Pearse (2012), Sombrero uplift above the Altiplano-Puna magma body: evidence of a ballooning mid-crustal diapir, *Science*, *338*, 250.

Folch, A., and J. Gottsmann (2006), Faults and ground uplift at active calderas, *Mechanisms of Activity and Unrest at Large Calderas. Geological Society, London, Special Publications*, *269*, 109–120.

Fossen, H. (2010), *Structural Geology*, Cambridge University Press, New York.

Fung, Y. C. (1965), *Foundations of Solid Mechanics*, Prentice-Hall, Englewood Cliffs.

Gercek, H. (2007), Poisson's ratio values for rocks, *International Journal of Rock Mechanics and Mining Sciences*, *44*(1), 1–13.

Geyer, A., and J. Gottsmann (2010), The influence of mechanical stiffness on caldera deformation and implications for the 1971-1984 Rabaul uplift (Papua New Guinea), *Tectonophysics*, *483*(3-4), 399–412.

Gottsmann, J., A. G. Camacho, J. Marti, L. Wooller, J. Fernandez, A. Garcia, and H. Rymer (2008), Shallow structure beneath the Central Volcanic Complex of Tenerife from new gravity data: Implications for its evolution and recent reactivation, *Physics of the Earth and Planetary Interiors*, *168*(3-4), 212–230.

Gudmundsson, A. (1990), Emplacement of dykes, sills and crustal magma chambers at divergent plate boundaries, *Tectonophysics*, *176*, 257–275.

Gudmundsson, A. (2002), Emplacement and arrest of sheets and dykes in central volcanoes, *J. Volcanol. Geotherm. Res.*, *116*, 279–298.

Gudmundsson, A. (2006), How local stresses control magma-chamber ruptures, dyke injections, and eruptions in composite volcanoes, *Earth-Science Reviews*, *79*(1-2), 1–31.

Gudmundsson, A. (2011), *Rock fractures in geological processes*, Cambridge University Press, New York.

Hanssen, R. F. (2001), *Radar interferometry: data interpretation and error analysis*, Kluwer Academic Publishers, Dordecht.

Hautmann, S., J. Gottsmann, R. S. J. Sparks, G. S. Mattioli, I. S. Sacks, and M. H. Strutt (2010), Effect of mechanical heterogeneity in arc crust on volcano deformation with application to Soufriere Hills Volcano, Montserrat, West Indies, *Journal of Geophysical Research-Solid Earth*, *115*, 18.

Isacks, B. L. (1988), Uplift of the central Andean plateau and bending of the Bolivian orocline, *Journal of Geophysical Research-Solid Earth and Planets*, *93*(B4), 3211–3231.

Jaeger, J. C., N. G. W. Cook, and R. W. Zimmerman (2007), *Fundamentals of Rock Mechanics*, Blackwell, Malden, Mass.

James, D. E. (1971), Plate tectonic model for the evolution of the Central Andes, *Geological Society of America Bulletin*, *82*, 3325–3346.

Jay, J., M. E. Pritchard, M. E. West, D. Christensen, M. Haney, E. Minaya, M. Sunagua, S. McNutt, and M. Zabala (2012), Shallow seismicity, triggered seismicity, and ambient noise tomography at the long-dormant Uturuncu Volcano, Bolivia, *Bull. Volcanol.*, *74*(4), 817–837.

Leidig, M., and G. Zandt (2003), Modelling of highly anisotropic crust and application to the Altiplano-Puna volcanic complex of the central Andes, *Journal of Geophysical Research-Solid Earth*, *108*(B1), ESE5-1–ESE5-15.

Manconi, A., T. R. Walter, and F. Amelung (2007), Effects of mechanical layering on volcano deformation, *Geophys. J. Int.*, *170*(2), 952–958.

Masterlark, T. (2007), Magma intrusion and deformation predictions: Sensitivities to the Mogi assumptions, *Journal of Geophysical Research-Solid Earth*, *112*(B6), BO6419.

McTigue, D. F. (1987), Elastic stress and deformation near a finite spherical magma body - resolution of the point-source paradox, *Journal of Geophysical Research-Solid Earth and Planets*, *92*(B12), 12931–12940.

Mogi, K. (1958), Relations between eruptions of various volcanoes and the deformations of the ground surfaces around them, *Bulletin of the Earthquake Research Institute*, *36*, 99–134.

Newman, A. V., T. H. Dixon, and N. Gourmelen (2006), A four-dimensional viscoelastic deformation model for Long Valley Caldera, California, between 1995 and 2000, *J. Volcanol. Geotherm. Res.*, *150*(1-3), 244–269.

Newman, A. V., T. H. Dixon, G. I. Ofoegbu, and J. E. Dixon (2001), Geodetic and seismic constraints on recent activity at Long Valley Caldera, California: evidence for viscoelastic rheology, *J. Volcanol. Geotherm. Res.*, *105*(3), 183–206.

Poland, M., M. Hamburger, and A. Newman (2006), The changing shapes of active volcanoes: History, evolution, and future challenges for volcano geodesy, *J. Volcanol. Geotherm. Res.*, *150*(1-3), 1–13.

Pritchard, M. E., and M. Simons (2002), A satellite geodetic survey of large-scale deformation of volcanic centers in the central Andes, *Nature*, *418*(6894), 167–171.

Pritchard, M. E., and M. Simons (2004), An InSAR-based survey of volcanic deformation in the central Andes, *Geochem. Geophys. Geosyst.*, *5*, 42.

Ranalli, G. (1995), *Rheology of the Earth*, Chapman and Hall, London.

Salisbury, M. J., B. R. Jicha, S. L. de Silva, B. S. Singer, N. C. Jimenez, and M. H. Ort (2011), Ar-40/Ar-39 chronostratigraphy of Altiplano-Puna volcanic complex ignimbrites reveals the development of a major magmatic province, *Geological Society of America Bulletin*, *123*(5-6), 821–840.

Scandura, D., A. Bonaccorso, G. Currenti, and C. Del Negro (2009), Thermo-mechanical modeling of ground deformation in volcanic areas, *Applied and Industrial Mathematics in Italy Iii*, *82*, 532–541.

Schilling, F. R., et al. (2006), Partial Melting in the Central Andean Crust: a review of geophysical, petrophysical and petrologic evidence, in *The Andes, Active Subduction Orogeny*, edited by O. Oncken, G. Chong, G. Franz, P. Giese, H.-J. Goetze, V. A. Ramos, M. R. Strecker and P. Wigger, pp. 459–474, Springer, Berlin.

Schmitz, M., W. D. Heinsohn, and F. R. Schilling (1997), Seismic, gravity and petrological evidence for partial melt beneath the thickened Central Andean crust (21-23 degrees S), *Tectonophysics*, *270*(3-4), 313–326.

Segall, P. (2010), *Earthquake and volcano deformation*, Princeton University Press, New Jersey.

Smith, R., P. R. Sammonds, and C. R. J. Kilburn (2009), Fracturing of volcanic systems: Experimental insights into pre-eruptive conditions, *Earth and Planetary Science Letters*, *280*(1-4), 211–219.

Sparks, R. S. J., C. B. Folkes, M. C. S. Humphreys, D. N. Barfod, J. Clavero, M. C. Sunagua, S. R. McNutt, and M. E. Pritchard (2008), Uturuncu volcano, Bolivia: Volcanic unrest due to mid-crustal magma intrusion, *Am. J. Sci.*, *308*(6), 727–769.

Springer, M., and A. Forster (1998), Heat-flow density across the Central Andean subduction zone, *Tectonophysics*, *291*, 123–139.

Trasatti, E., C. Giunchi, and M. Bonafede (2005), Structural and rheological constraints on source depth and overpressure estimates at the Campi Flegrei caldera, Italy, *J. Volcanol. Geotherm. Res.*, *144*(1-4), 105–118.

Wigger, P. J., et al. (1994), Variation in crustal structure of the southern Central Andes deduced from seismic refraction investigations, in *Tectonics of the Southern Central Andes: Structure and Evolution of an Active Continental Margin*, edited by K.-J. Reutter, E. Scheuber, and P. J. Wigger, pp. 23–48, Springer-Verlag, New York.

Williams, C. A., and G. Wadge (1998), The effects of topography on magma chamber deformation models: Application to Mt Etna and radar interferometry, *Geophys. Res. Lett.*, *25*(10), 1549–1552.

Yang, X. M., P. M. Davis, and J. H. Dieterich (1988), Deformation from inflation of a dipping finite prolate spheroid in an elastic half-space as a model for volcanic stressing, *Journal of Geophysical Research-Solid Earth and Planets*, *93*(B5), 4249–4257.

Yuan, X., et al. (2000), Subduction and collision processes in the Central Andes constrained by converted seismic phases, *Nature*, *408*(6815), 958–961.

Yun, S., P. Segall, and H. Zebker (2006), Constraints on magma chamber geometry at Sierra Negra Volcano, Galápagos Islands, based on InSAR observations, *J. Volcanol. Geotherm. Res.*, *150*, 232–243.

Zandt, G., M. Leidig, J. Chmielowski, D. Baumont, and X. H. Yuan (2003), Seismic detection and characterization of the Altiplano-Puna magma body, central Andes, *Pure and Applied Geophysics*, *160*(3-4), 789–807.

Zhang, Z. X. (2002), An empirical relation between mode I fracture toughness and the tensile strength of rock, *International Journal or Rock Mechanics and Mining Sciences*, *39*(3), 401–406.